Supporting information

Heterostructured Bi-Cu_2S Nanocrystals for Efficient CO_2 Electroreduction to Formate

Xue Han, [a] Tianyou Mou, [a] Shikai Liu, [b] Mengxia Ji, [a,c] Qiang Gao, [a] Qian He, [b] Hongliang Xin, [a] and Huiyuan Zhu *[a]

[a] Department of Chemical Engineering, Virginia Polytechnic Institute and State University, Blacksburg, Virginia 24061, United States. E-mail: huiyuanz@vt.edu

[b] Department of Materials Science and Engineering, National University of Singapore, 117575, Singapore

[c] Institute of Energy Research, Jiangsu University, Zhenjiang, 212013, P. R. China.

Experimental Section

Materials. Bismuth acetate (Bi(ac)$_3$, >99.99%), copper(II) acetylacetonate (Cu(acac)$_2$, 99.99%), bismuth neodecanoate, oleylamine (OAm, 70%), 1-octadecene (ODE, 90%), 1,2,3,4-tetrahydronaphthalene (Tetralin), 1-dodecanethiol (DDT, >98%), tert-dodecanethiol (t-DDT), trioctylphosphine oxide (TOPO), trioctylphosphine (TOP), potassium bicarbonate (KHCO$_3$, 99.7%), 3-(trimethylsilyl) propionic-2,2,3,3-d$_4$ acid sodium salt (NMR standard) and nafion perfluorinated resin solution (5 wt%) were purchased from Sigma-Aldrich. The Nafion-117 membrane, Vulcan XC carbon black and AvCarb carbon paper were purchased from FuelCellStore. All chemicals were used as-received without further purification. Argon (99.99%), carbon dioxide (99.999%) were purchased from Airgas.

Synthesis of heterostructured Bi-Cu$_2$S nanocrystals. 1 mmol of Bi(ac)$_3$, 1 mmol Cu(acac)$_2$, and 9.5 ml OAm were added into a 50 mL four-necked flask under magnetic stirring. The mixture was heated to 140 °C and kept at this temperature for 2 h under nitrogen (N$_2$) flow to remove dissolved moisture and oxygen. Then the mixture was heated to 220 °C at a ramping rate of 7 °C min^{-1}, while 0.5 mL OAm and 0.24 mL DDT were well-mixed and injected into the solution to induce the formation of sulfide. The reaction solution was kept at this temperature for 30 min. After being cooled to room temperature, the product was collected and purified by excessive ethanol by centrifuging at 800 rpm for 1 min to remove the remaining precursor and impurities. The product was further centrifuged at 5500 rpm for 5 min and washed twice with ethanol and redispersed in hexane for further use.

Synthesis of Bi NPs. The synthesis procedure of Bi NPs was similar to a previously reported method.[1] Typically, 1 mmol bismuth neodecanoate was mixed with 10 mL Tetralin and heated to 110 °C and incubated for 30 min under the N$_2$ flow. The solution then cooled down to 80 °C, while 0.24 mL DDT was injected into the solution. After the DDT injection, 1 mL TOP was injected into the solution and the system was further cooled down to 70 °C and kept at this temperature for 30 min. The final products were collected and centrifuged, followed by washing with ethanol for 3 times.

Synthesis of Cu$_2$S NRs. The synthesis procedure of Cu$_2$S NRs was similar to a previously reported method.[2] 0.5 mmol Cu(acac)$_2$, 2.5 mmol TOPO were mixed with 10 mL ODE and heated up to 80 °C and kept there for 30 min under the N$_2$ flow. Then, the mixture was heated up to 180 °C in 5 min while 2.5 mL t-DDT was injected at 120 °C. The reaction solution was kept at 180 °C for 15 min. The final products were collected and centrifuged, followed by washing with ethanol for 3 times.

The physical mixture of Bi NPs and Cu$_2$S NRs (Bi NPs+Cu$_2$S NRs). 7.5 mg Bi NPs and 2.5 mg Cu$_2$S NRs were weighed and mixed in the hexane. The mixture was sonicated for 2 h and then stirred overnight to achieve a homogeneous solution. The product was then centrifuged and redispersed in hexane for further use.

Characterizations. The morphology and sizes of the Bi-Cu$_2$S heterostructures, Bi NPs, and Cu$_2$S NRs were characterized by the transmission electron microscopy (TEM) on Philips EM420 operated at 120 kV. High-resolution TEM (HRTEM), high-angle annular dark-field scanning TEM (STEM-HAADF), X-ray energy dispersive spectroscopy (X-EDS) and EDS mapping were conducted on a JEOL ARM 200CF equipped with an Oxford Instrument X-ray Energy Dispersive Spectrometer. X-ray diffraction (XRD) patterns were collected by a Philips X'Pert Pro Super with Cu Kα (λ=1.5406 Å). The X-ray photoelectron spectroscopy (XPS) was collected on a PHI Versa probe III microscopy with Al Kα monochromatic energy source at 1486.6 eV. Inductively coupled plasma optical emission spectroscopy (ICP-OES) was performed for the quantitative analysis of the elemental contents on a SPECTRO GENESIS ICP spectrometer.

Catalyst preparation and surfactant removal. To load Bi-Cu$_2$S on carbon (Bi-Cu$_2$S/C), 10 mg as-synthesized Bi-Cu$_2$S heterostructures were sonicated with 40 mg activated carbon (Vulcan XC-72R) in hexane for 2 h. The products were then collected by centrifugation at 8500 rpm for 5 min. The removal of organic ligands was achieved by immersing the catalysts in a mixture of 1.5 mL hydrazine and 18.5 mL ethanol overnight and washing with excessive ethanol twice. The final products were dried for 4 h in the vacuum oven at 50 °C. The Bi/C, Cu_2S/C, and Bi+Cu_2S/C were also prepared following the same procedure.

Electrochemical measurements and product analysis. Electrochemical measurements were all carried out in 0.1 M $KHCO_3$. To prepare the working electrode, 10 mg of Bi-Cu_2S/C catalyst powder was mixed with 2 mL isopropanol and 40 μL of Nafion solution (5 wt%, Sigma-Aldrich) by sonicating for 30 min to achieve a homogeneous catalyst ink. This catalyst ink was then airbrushed onto a carbon paper with an area of 1x1 cm^2 and was naturally dried before use. The loading amount was calculated by weighing the carbon paper before and after the airbrushing, achieving the Bi-Cu_2S/C loading of 1 mg cm^{-2}. All the potentials were controlled via a Biologic electrochemical workstation. The H-type gas-tight cell was separated by a Nafion (117) membrane, and each compartment contained a 40 mL electrolyte. The cathodic compartment was housed the working electrode and the reference electrode (Ag/AgCl, 3.5 M KCl), while the anodic compartment contained a platinum foil as the counter electrode. Cyclic voltammograms (CVs) were recorded in Ar-saturated 0.1 M $KHCO_3$ between -1.8 V and -0.6 V vs. Ag/AgCl after 10 cycles with a scan rate of 20 mV s^{-1} at room temperature and then recorded in CO_2-saturated electrolyte under the same condition. Linear sweep voltammograms (LSVs) were measured from -0.6 V to -1.8 V vs. Ag/AgCl with a scan rate of 20 mV s^{-1} in CO_2-saturated 0.1 M $KHCO_3$. Chronoamperometry (CA) measurements were performed at each potential from -1.4 V to -1.8 V vs. Ag/AgCl for 1 h in the H-type cell system. All the potentials were then converted to the reversible hydrogen electrode (RHE) reference scale by the following equation:

$$E(vs. RHE) = E(vs. Ag/AgCl) + 0.21\ V + 0.0591 \times pH$$

Before the test, the catholyte was purged with CO_2 for 30 min to remove residual air. Then, a consistent CO_2 flow was introduced to the cathodic compartment at a flow rate of 10 sccm during the electrolysis. The gaseous products were analyzed *via* online gas chromatography (GC, Agilent 7890 B). After the electrochemical reactions, the cathodic electrolyte was collected to analyze the liquid products by nuclear magnetic resonance spectroscopy (NMR, Bruker Avance II 500Hz).

The calculation of Faradic efficiency

The Faradic efficiency (FE) of gas products were calculated by:

$$J_{CO} = \frac{A}{\alpha} \times V_{CO_2} \times \frac{2Fp_0}{RT} \times (Electrode\ area)^{-1}$$

$$J_{H_2} = \frac{B}{\beta} \times V_{CO_2} \times \frac{2Fp_0}{RT} \times (Electrode\ area)^{-1}$$

where α and β are the conversion factors based on the calibration of the GC with the standard samples of CO and H_2, respectively. V_{CO_2} is the flow rate of CO_2 (10 sccm); F is the Faradic constant (96485 C mol^{-1}); p_0 is the pressure (1 atm); T is the temperature (273 K); R is the gas constant (82.1 mL atm K^{-1} mol^{-1}); A and B are the peak areas of CO and H_2 obtained from GC. FE for the various gas products was obtained by dividing the partial current density by the total current density.[3-4]

The liquid product was analyzed by NMR. To prepare the NMR sample, 0.5 mL electrolyte containing the liquid product ($HCOO^-$) was mixed with 0.1 mL D_2O and 0.1 mL 0.1 M 3-(trimethylsilyl) propionic-2,2,3,3-d_4 acid sodium salt (internal standard). The FE of liquid-phase product was calculated by:

$$FE_{HCOO^-}(\%) = \frac{2nF}{It} \times 100$$

where n is the moles of formate, calculating from the calibration curve of the NMR. F is the Faradic constant (96485 C mol^{-1}). I is the applied current (A) and t is the electrolysis time (s).

The error bars in the figures are based on the average value of three repeated experiments.

The production rate of formate over Bi-Cu_2S and Bi was calculated after 1 h electrolysis at each given potentials.

Experimental Supporting figures

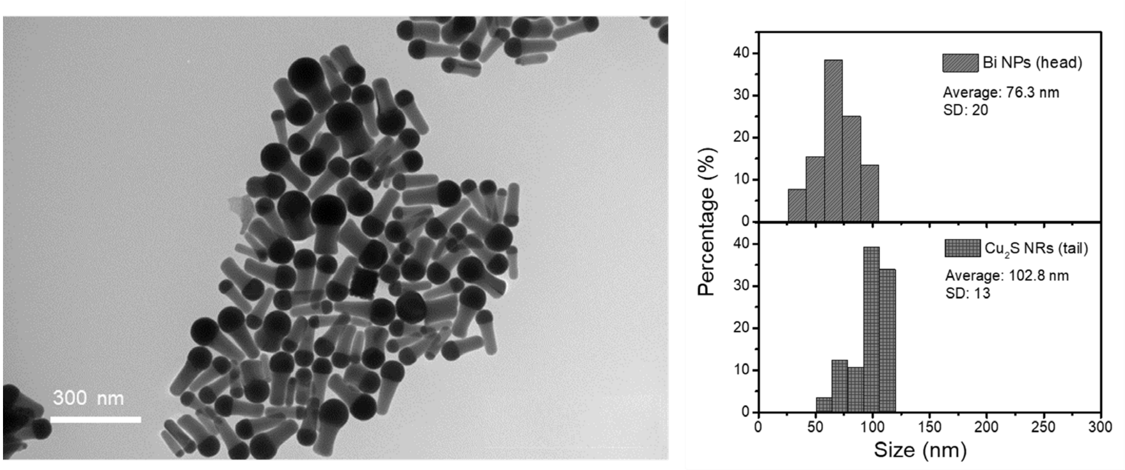

Figure S1. The low magnification TEM image and size distribution with average size and standard deviation (SD) of Bi-Cu_2S nanocrystals.

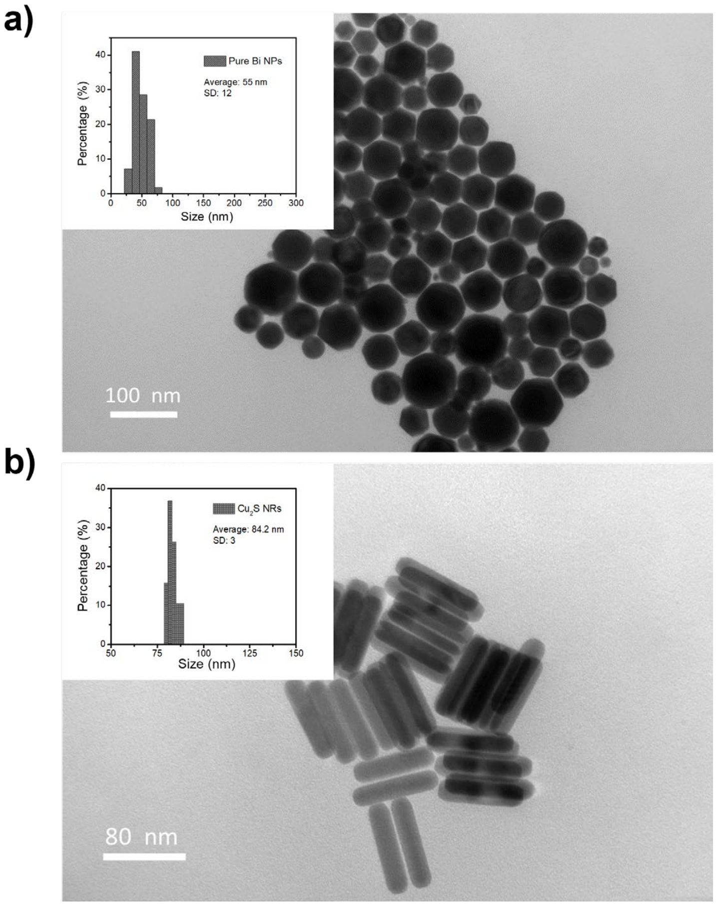

Figure S2. TEM images and size distribution with average size and standard deviation (SD) of (**a**) Bi NPs and (**b**) Cu$_2$S NRs.

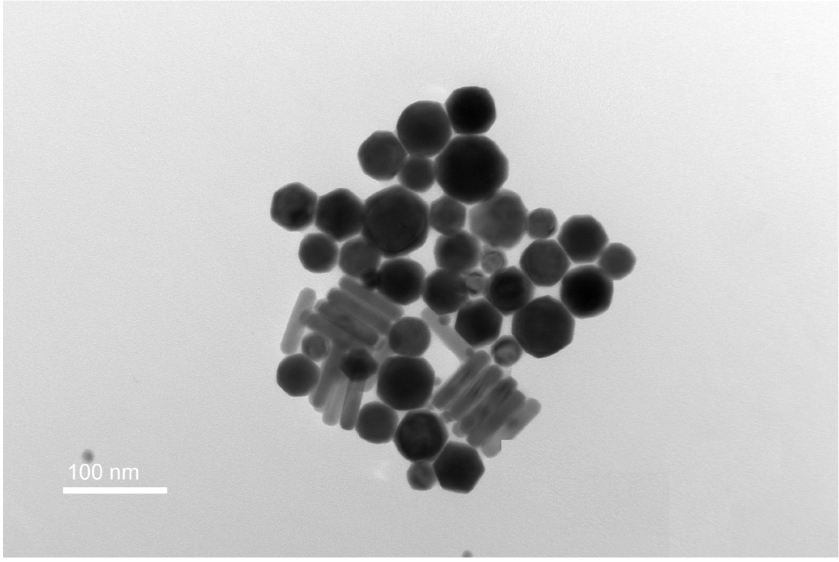

Figure S3. The TEM image of the physical mixture of Bi NPs and Cu_2S NRs.

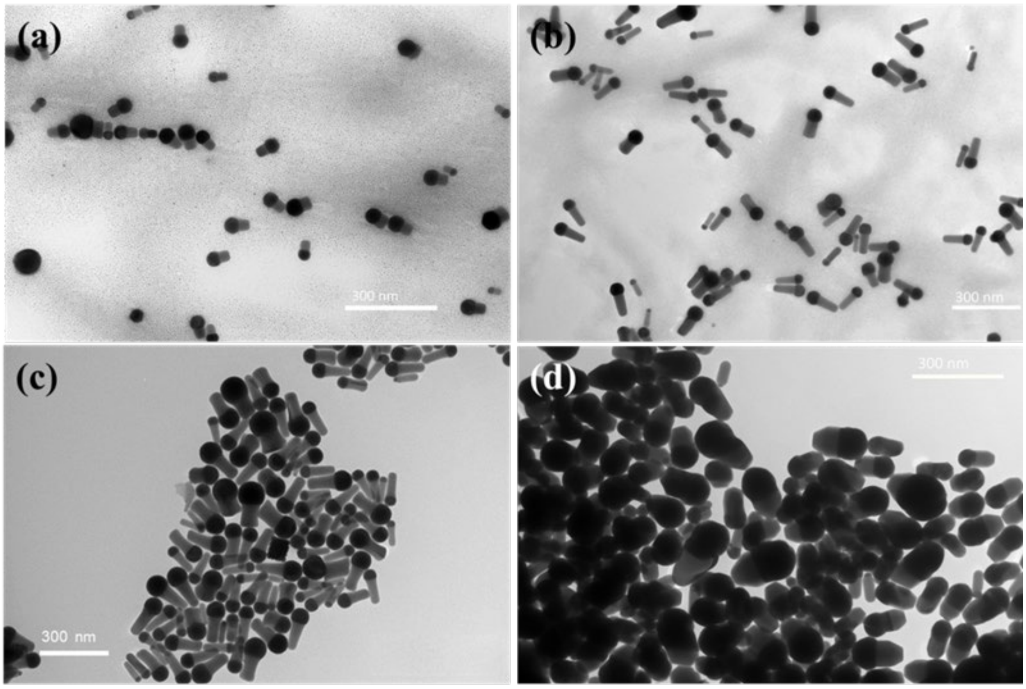

Figure S4. TEM images of Bi-Cu_2S heterostructures with different reaction time: a) 5 min; b) 15 min; c) 30 min; d) 120 min.

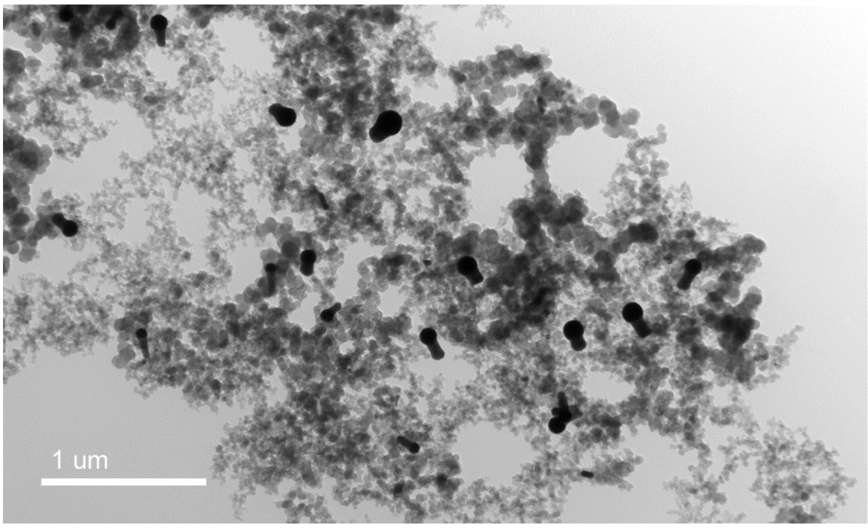

Figure S5. The TEM image of Bi-Cu_2S/C.

After the ECO_2RR (**Figure S6c**), the Cu 2p spectra of Bi-Cu_2S show two Cu $2p_{3/2}$ features at 932.3 and 933.7 eV, which can be assigned to Cu^{1+} and Cu^{2+}, respectively. As shown in the Cu 2p spectra, the ratio of Cu^{2+}/Cu^{1+} slightly increases after the ECO_2RR. In Cu 2p XPS spectra of Cu_2S NRs (**Figure S8c, d**), Cu^{1+} and Cu^{2+} are also observed and the ratio of Cu^{2+}/Cu^{1+} increases after the ECO_2RR. This can be attributed to the partial reduction of Cu^{1+} to the metallic Cu^0 during the reduction and its subsequent natural oxidation to CuO during the sample processing for XPS analysis.

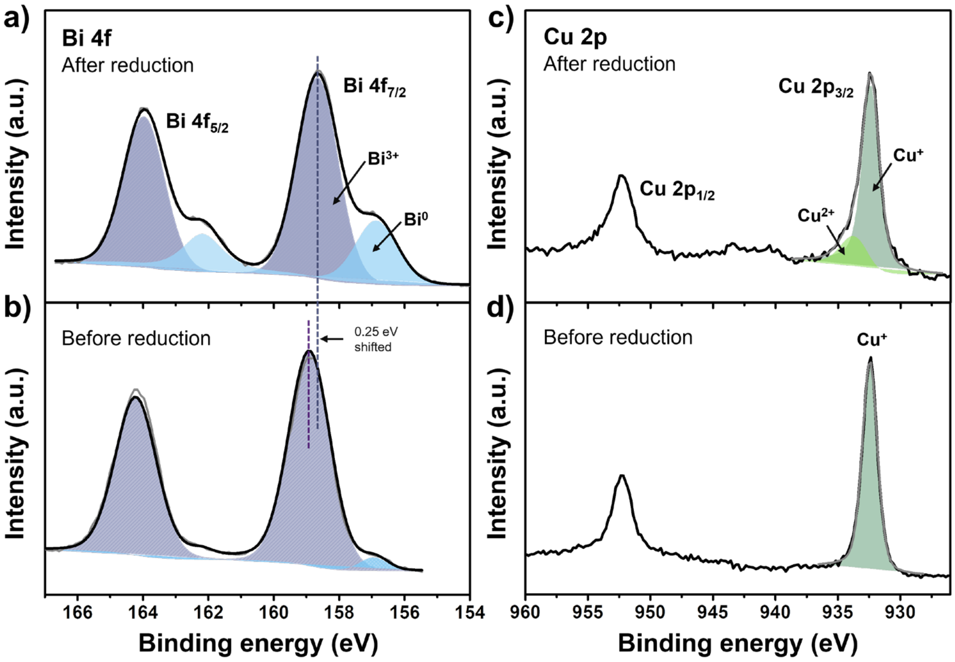

Figure S6. Bi 4f XPS spectra of Bi-Cu_2S after (**a**) and before (**b**) the ECO_2RR; Cu 2p XPS spectra of Bi-Cu_2S after (**c**) and before (**d**) the ECO_2RR.

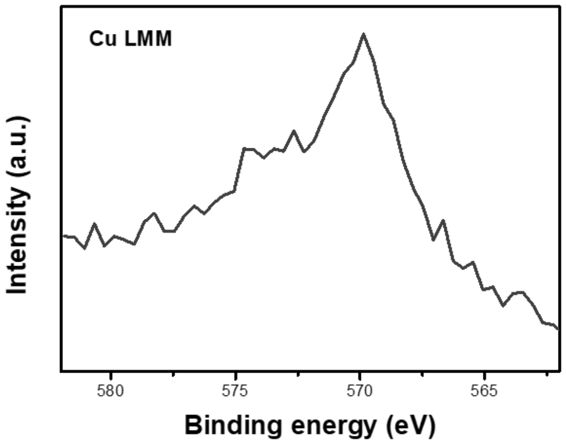

Figure S7. XPS Cu LMM Auger spectrum of Bi-Cu_2S.

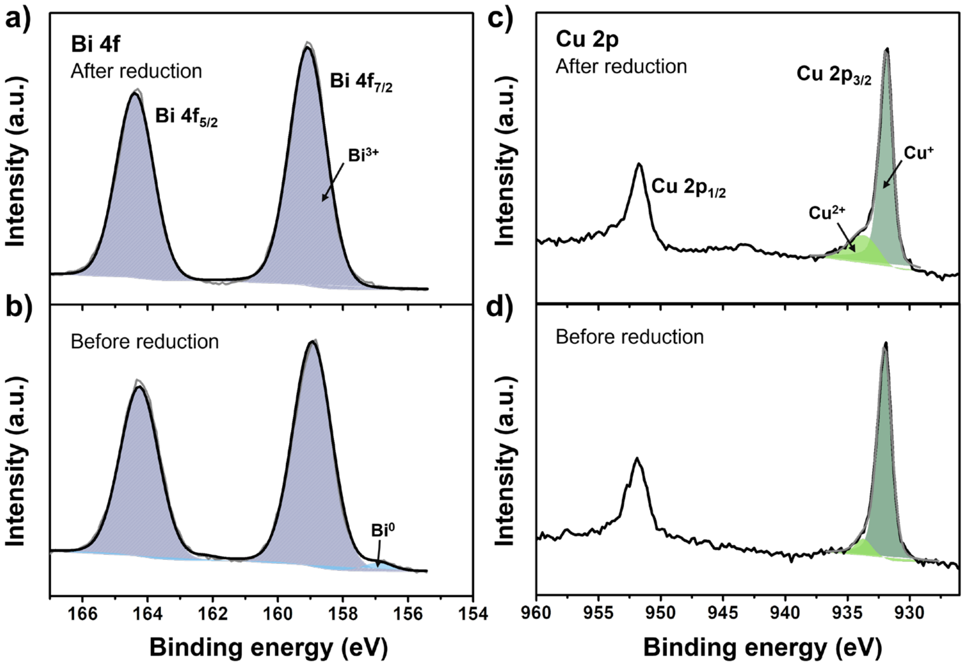

Figure S8. Bi 4f XPS spectra of Bi NPs (**a**) after the ECO_2RR measurement and (**b**) before the ECO_2RR measurement; Cu 2p XPS spectra of Cu_2S NRs (**c**) after the ECO_2RR measurement and (**d**) before the ECO_2RR measurement.

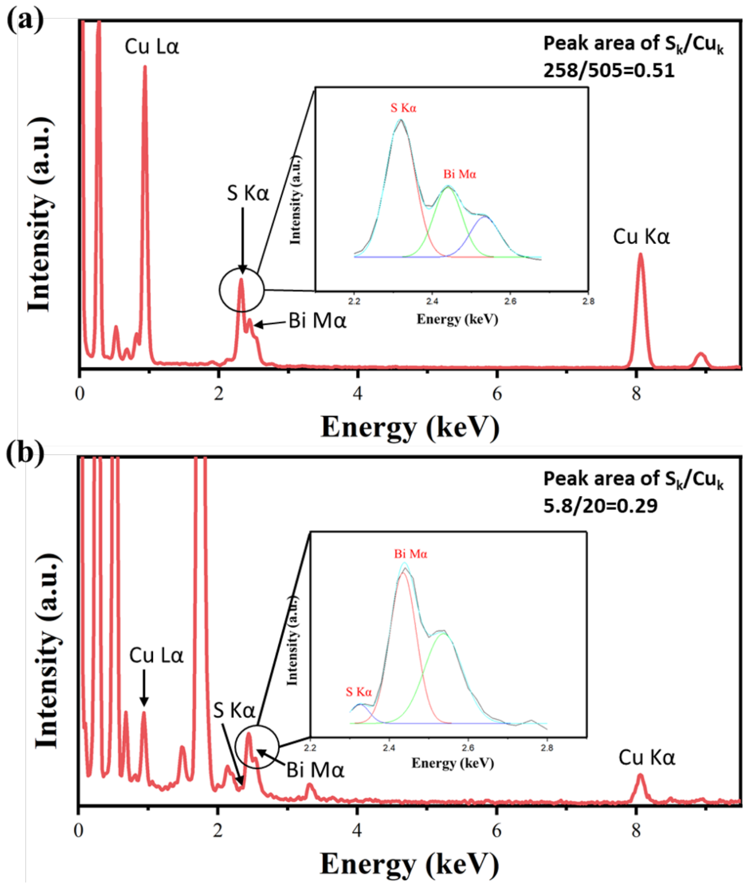

Figure S9. EDS spectra of Bi-Cu_2S heterostructures: **a**) before and **b**) after 5 hours of ECO_2RR.

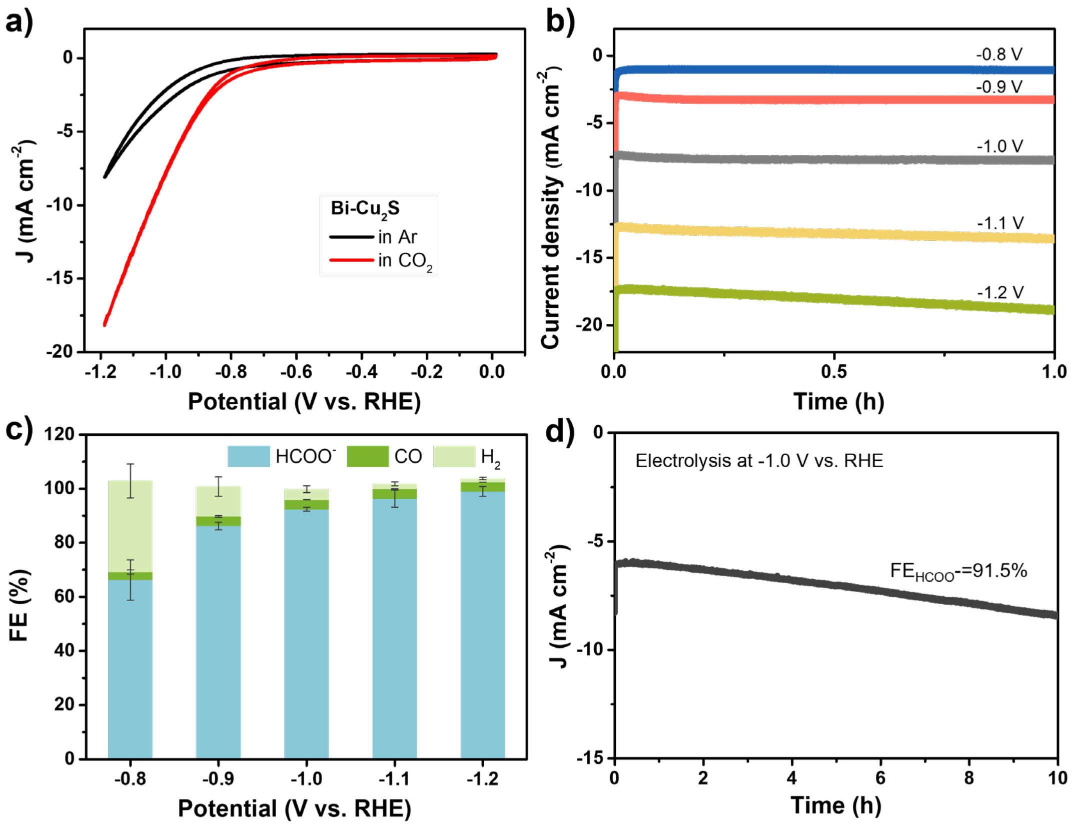

Figure S10. The ECO$_2$RR performance on Bi-Cu$_2$S catalyst: **a)** CV curves in Ar-saturated (black line) and CO$_2$-saturated (red line) 0.1 M KHCO$_3$ normalized to geometric area. **b)** Current density over 1 h of electrolysis at each given potential (-0.8 to -1.2 V vs. RHE). **c)** FE for ECO$_2$RR at various applied potentials. **d)** Durability test at -1.0 V for 10 h.

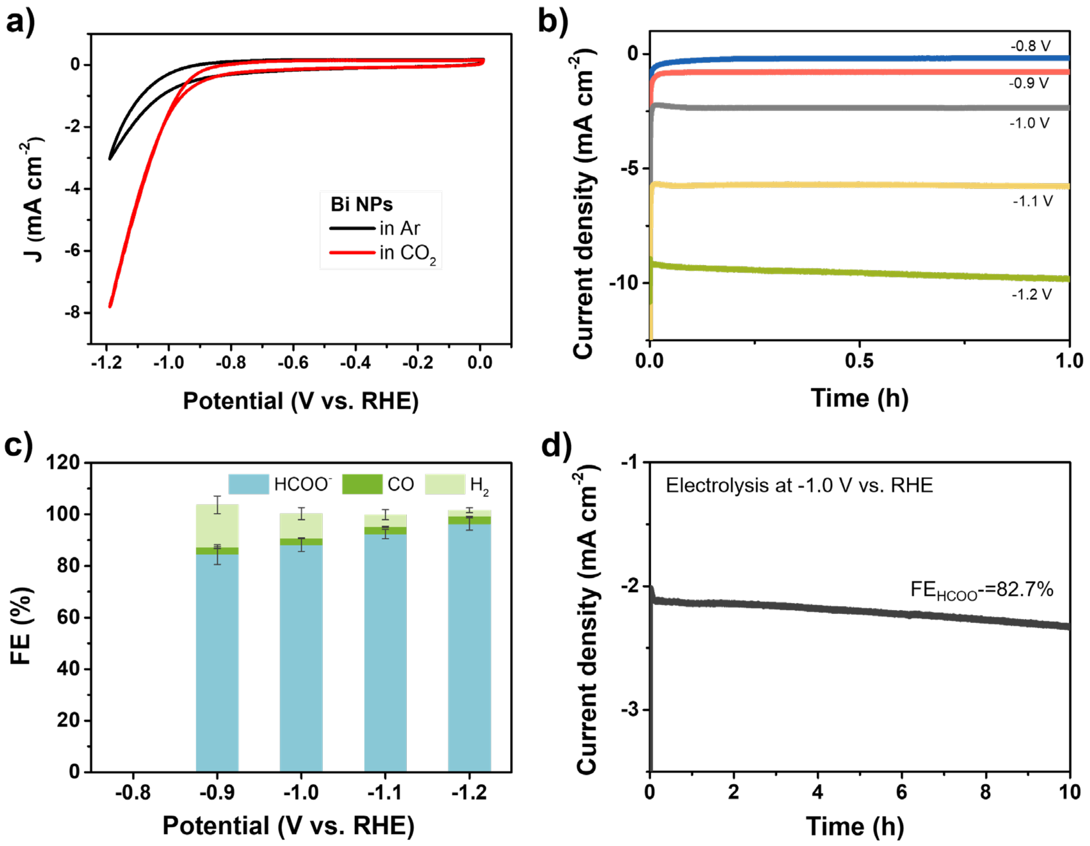

Figure S11. The ECO_2RR performance on Bi NPs: **a)** CV curves in Ar-saturated (black line) and CO_2-saturated (red line) 0.1 M $KHCO_3$ normalized to geometric area. **b)** Current density over 1 h of electrolysis at each given potential (-0.8 to -1.2 V vs. RHE). **c)** FE for ECO_2RR at various applied potentials. **d)** Durability test at -1.0 V for 10 h.

]

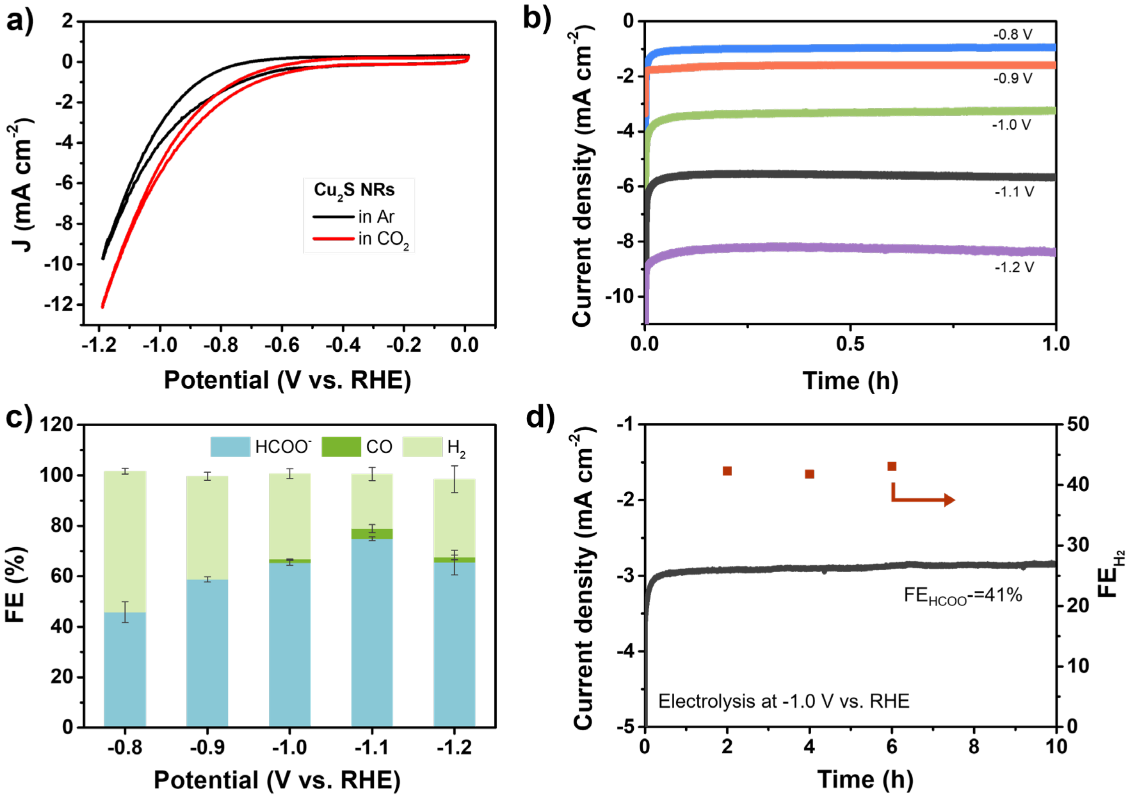

Figure S12. The ECO_2RR performance on Cu_2S NRs: **a)** CV curves in Ar-saturated (black line) and CO_2-saturated (red line) 0.1 M $KHCO_3$ normalized to geometric area. **b)** Current density over 1 h of electrolysis at each given potential (-0.8 to -1.2 V vs. RHE). **c)** FE for ECO_2RR at various applied potentials. **d)** Durability test at -1.0 V for 10 h.

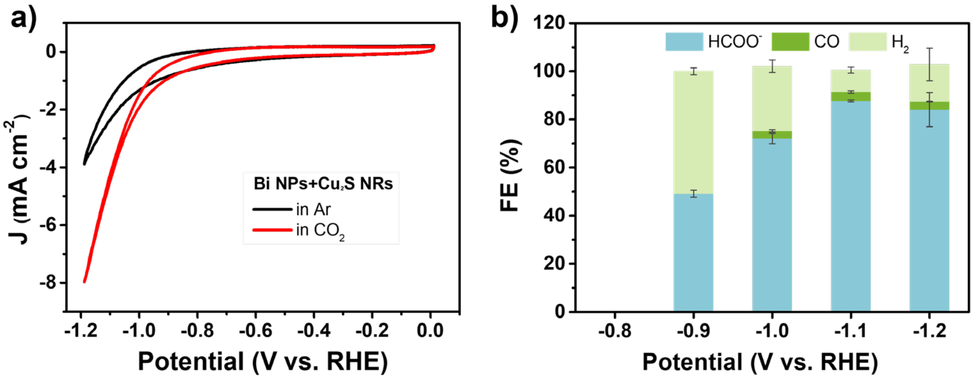

Figure S13. The ECO$_2$RR performance on the mixture of Bi NPs and Cu$_2$S NRs (Bi NPs+Cu$_2$S NRs): (**a**) CV curves in Ar-saturated (black line) and CO$_2$-saturated (red line) 0.1 M KHCO$_3$ normalized to geometric area. (**b**) FE for ECO$_2$RR at various applied potentials.

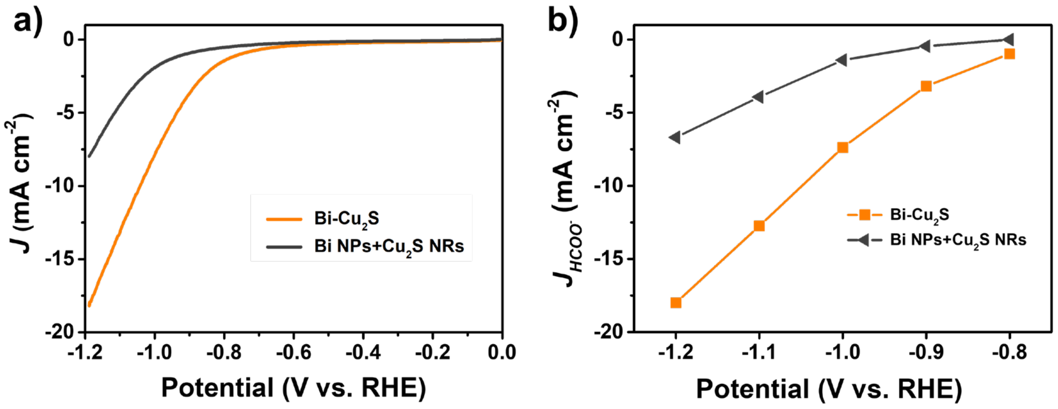

Figure S14. a) LSV of Bi-Cu$_2$S, and Bi NPs+Cu$_2$S NRs mixed sample in CO$_2$-saturated 0.1 M KHCO$_3$ normalized to geometric area. **b**) Partial current density of formate obtained on Bi-Cu$_2$S and Bi NPs+Cu$_2$S NRs mixed sample at different potentials in CO$_2$-saturated 0.1 M KHCO$_3$ electrolyte.

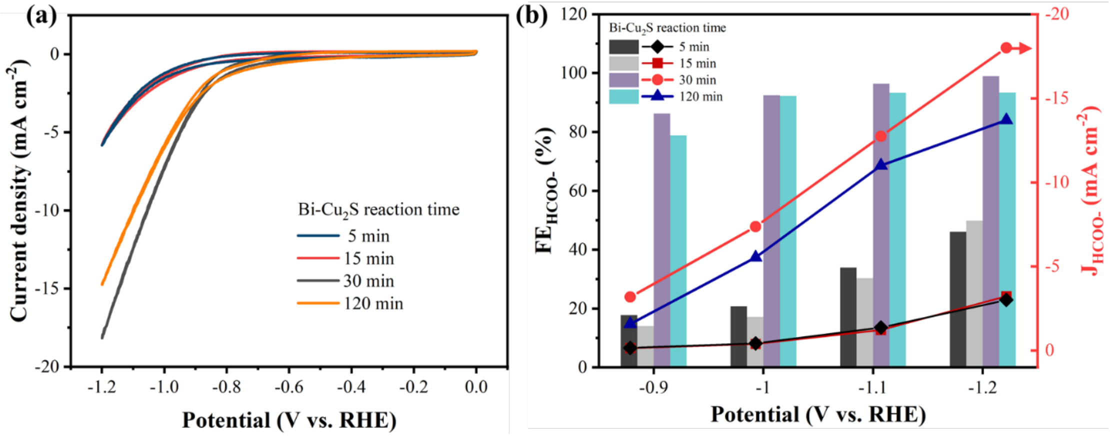

Figure S15. Electrochemical CO_2 reduction reaction on Bi-Cu_2S/5, Bi-Cu_2S/15, Bi-Cu_2S/30, and Bi-Cu_2S/120 in the CO_2-saturated 0.1 M $KHCO_3$ electrolyte: (a) CV curves; (b) Partial current density and FE on formate production at different potentials.

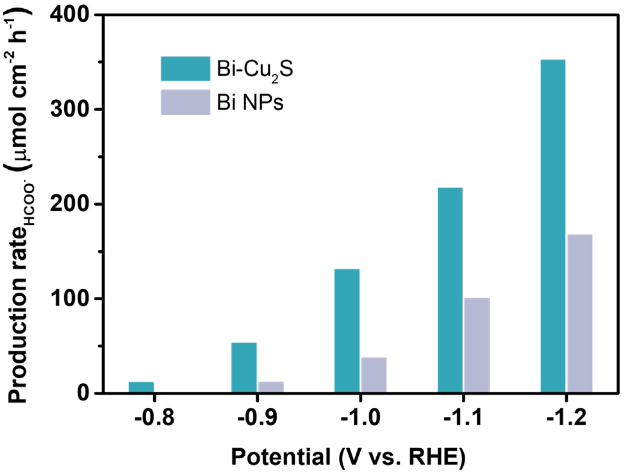

Figure S16. The production rate of formate from ECO$_2$RR on Bi-Cu$_2$S and Bi at various potentials.

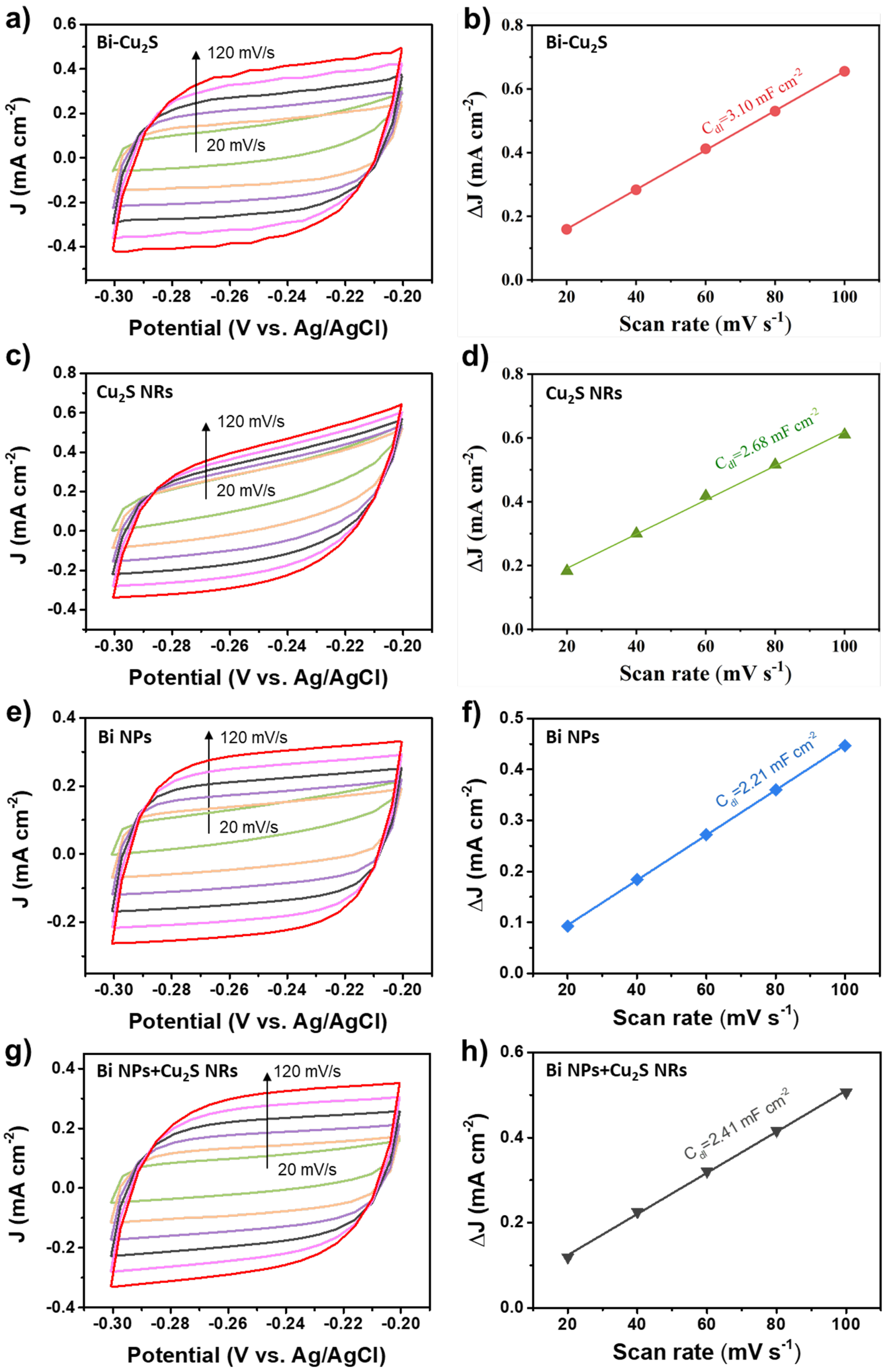

Figure S17. Electrochemical surface area (ECSA) measured by CV cycling in Ar-saturated 0.1 M $KHCO_3$, and their linear fitting for **a) b)** Bi-Cu_2S; **c) d)** Cu_2S NRs; **e) f)** Bi NPs; **g) h)** The mixture of Bi NPs and Cu_2S NRs (Bi NPs + Cu_2S NRs).

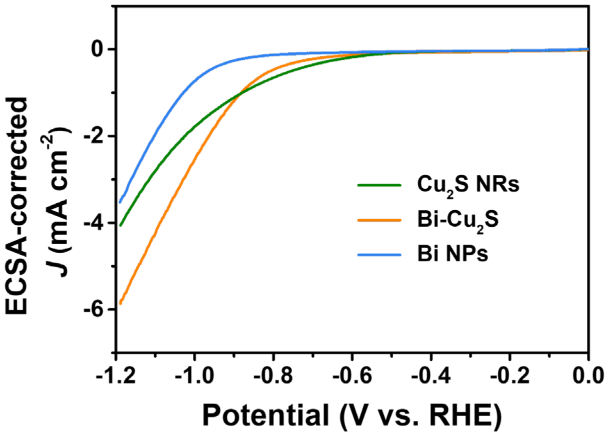

Figure S18. ECSA-corrected total current densities on Bi-Cu_2S, Cu_2S NRs, and Bi NPs.

Computational Details

DFT calculation settings

All density functional theory (DFT) calculations were performed using Vienna Ab initio Simulation Package (VASP), interfaced with the Atomic Simulation Environment. The ion-electron interactions were described by the projector-augmented plane-wave approach. The Perdew-Burke-Ernzerhof generalized gradient approximation was selected as the description of the exchange and correlation interactions. In this work, two model systems including Bi (001) and Bi (001) with a Cu_2S nanorod were constructed. For both systems, Bi (001) was represented by 3 layers of a 3×3 supercell with a lattice parameter of a = b = 4.586 Å. For Bi-Cu_2S interfacial system, 3 layers of a 2×2 supercell of Cu_2S (100) slab with lattice parameters of a = 3.890 Å and c/a = 1.768 Å were used as a nanorod on top of the same Bi (001) substrate (**Figure S19**). All lattice parameters agree with experimental results and literature values within 1% error[5-6]. The adsorbates and top two layers including the Cu_2S clusters were fully relaxed until the energy and interatomic forces were minimized down to 1×10^{-5} eV and 0.03 eV/Å, respectively. The bottom four layers were fixed in their bulk positions. The slab was separated with 15 Å of vacuum space to avoid interactions in the periodic calculations in the z direction. The cutoff energy was 420 eV for plane-wave basis sets with Fermi-level smearing of 0.05 eV for slabs and 0.01 eV for gas species. Free formation energies were calculated as:

$$G = E_{DFT} + E_{ZPE} - TS$$

where E_{DFT}, E_{ZPE}, TS were electronic energy, zero-point energy, entropy contribution, respectively. For adsorbates, E_{ZPE} and S were determined by vibrational frequency calculations, with all 3N degrees of freedom treated as harmonic vibrational motions (<50 cm^{-1} ones are replaced by 50 cm^{-1}). For molecules, all thermodynamic values were taken from the tabulated NIST database[7]. DFT electronic energies for some molecules were corrected by combining with the experimental values since the inaccuracy of the PBE functional in describing these molecules[8-9]. $HCOO^-(aq)$ energy is calculated directly from the experimental reduction potential of CO_2 to $HCOO^-(aq)$, *i.e.*, -0.43 V vs. SHE at pH=7. The solvation effect on adsorbates was considered as an *ad hoc* effect and taken from literature values[10-11]. All contributions to the Gibbs free energy were provided in **Table S1**.

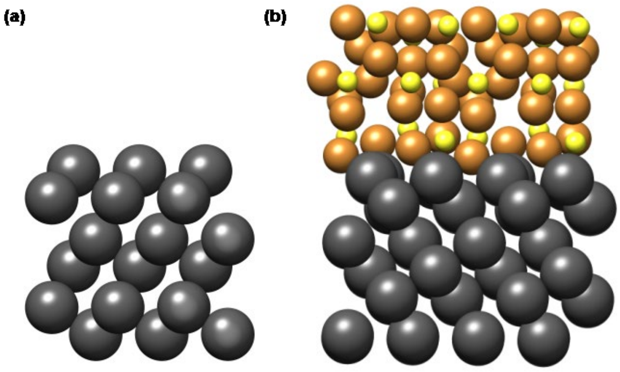

Figure S19. Front view of **(a)** Bi (001) surface and **(b)** Bi-Cu_2S interfacial model surface.

Table S1. Thermodynamics of free molecules and surface species[a]

Molecules	ZPE	-TS	Gas phase correction	Solvation
$H_2(g)$	0.27	-0.41	-	-
$H_2O(g)$	0.56	-0.67	-	-
CO_2 (g)	0.31	-0.66	0.17	-
H_2S (g)	0.40	-0.64	-	-
CO (g)	0.13	-0.61	-0.24	-
*H	0.14	-0.03		0.01
*COOH	0.59	-0.29		-0.29
*OCHO	0.59	-0.33		-0.23

[a]All values are in electronvolt (eV). Temperature was set to 298.15K.

The computational hydrogen electrode (CHE) model was employed to determine the free energy change of electrochemical elementary steps. All proton and electron transfers were assumed to be coupled. At 0 V vs RHE and 298.15 K, protons and electrons are at equilibrium with 1 bar of H_2 at arbitrary pH:

$$H^+ + e^- \rightarrow 1/2H_2$$

At any given potential U, the energy of e^- will be shifted by $-eU$[12-13]. For example, the free energy of the reaction:

$$CO_2 + H^+ + e^- \rightarrow * OCHO$$

would be calculated by:

$$\Delta G = G_{*OCHO} - G_{CO2} - [\frac{1}{2}G_{H2} - eU]$$

Cu_2S hypothetical structure

Cu_2S forms multiple phases depending on the reaction conditions. The synthesis temperature in this work is between 103°C and 450°C, a hexagonal crystal structure also named as high chalcocite is generated. However, this high chalcocite structure is found to have a high mobility of Cu atoms and only sulfur atoms stay at lattice points of the hexagonal lattice. For simplicity of the modeling, a hypothetical structure used in previous studies[14-15] has been employed to model the nanorod on top of the Bi surface. The property of the hypothetical structure was confirmed to be consistent with the real structure[16]. The coordinates of elements in the Cu_2S unit cell and the crystal information are listed in **Table S2**, while the crystal structure is shown in **Figure S20**.

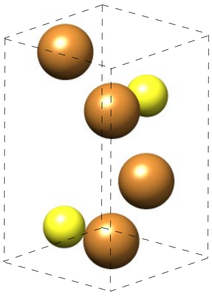

Figure S20. Cu_2S unit cell

Table S2. Cu_2S atomic coordinates

Elements	Coordinate (relative to unit cell)		
	x	y	z
S	1/3	2/3	1/4
Cu (1)	0	0	1/4
Cu (2)	1/3	2/3	0.578

Sulfur vacancy free formation energy

Sulfur vacancy free formation energy is calculated using a 2×2 supercell of Cu_2S (001) surface and is given by,

$$E_v^S = E(Defect\ surface) - E(Pristine\ surface) + E(H_2S) - E(H_2)$$

Where $E(Defect\ surface)$, $E(Pristine\ surface)$, $E(H_2S)$, $E(H_2)$ are the DFT total energies of the defect cell, pristine cell, H_2S molecule and H_2 molecule, respectively. The operating potential U vs. pH was plotted in **Figure 4b**. The red line is the potential U at which the vacancy starts to form. When the potential is more negative than the red line, the vacancy formation energy is negative which indicates the feasibility of losing sulfur atoms on the surface. The reaction operating conditions is plotted by the black line, starting from -1.21 V to -1.61 V vs. SHE at pH=7, and at this condition vacancies are formed on the surface.

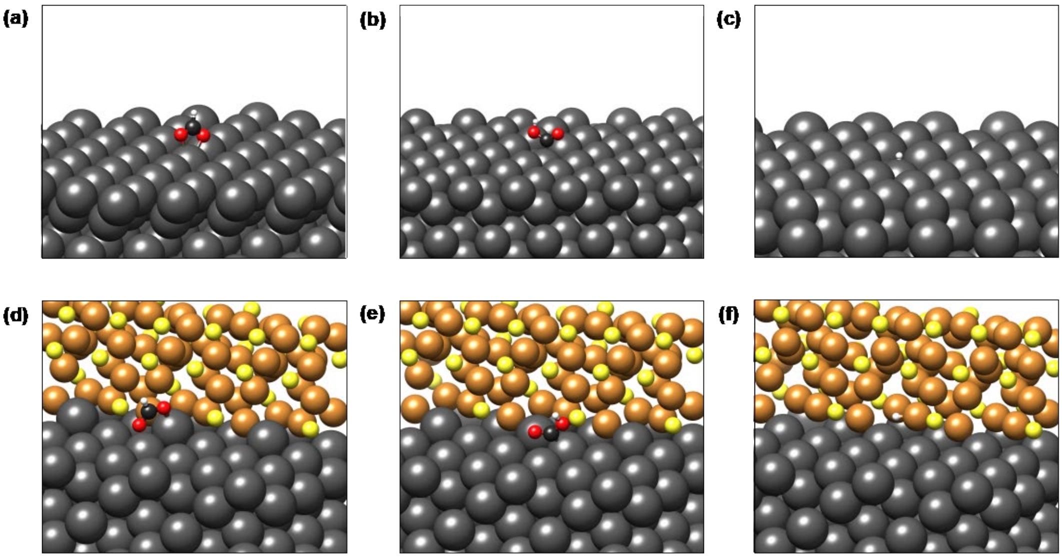

Figure S21. Adsorption geometries of (**a**) *OCHO, (**b**) *COOH, and (**c**) *H on Bi (001) surface, and adsorption geometries of (**d**) *OCHO, (**e**) *COOH, and (**f**) *H on Bi-Cu_2S interfacial system.

Charge density difference calculation

The charge density differences were generated by the differences for the charge density, ρ, of various systems with adsorbates (*OCHO, *COOH and *H) and two reference systems: a bare surface system and radicals of adsorbates (OCHO, COOH and H)

$$\Delta\rho = \rho_{All} - \rho_{slab} - \rho_{adsorbate}$$

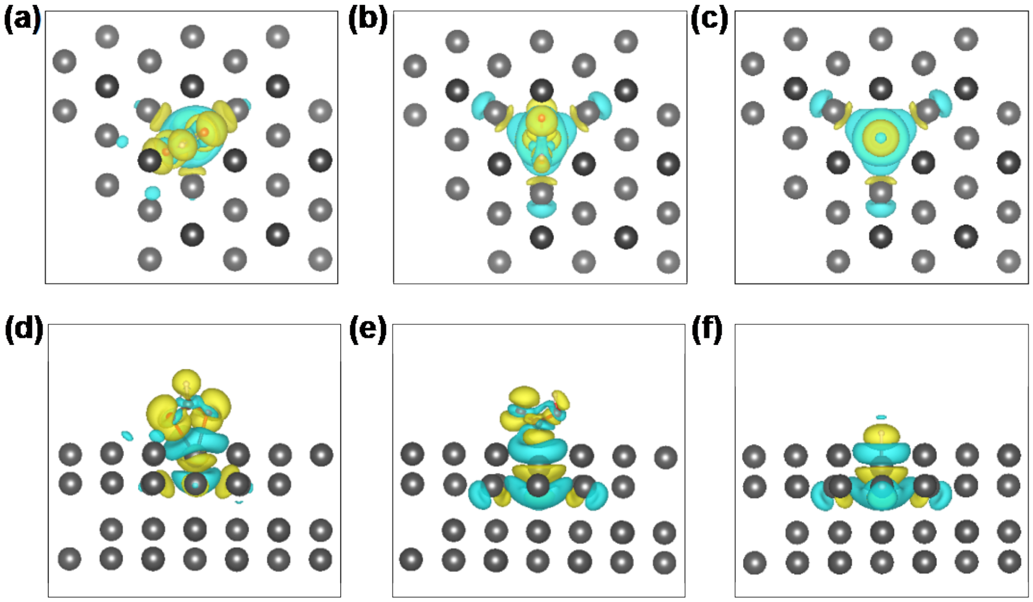

Figure S22. Isosurfaces of adsorbate-induced charge density difference for adsorbates on Bi (001). **(a)**, **(b)**, and **(c)** are top views of *OCHO, *COOH, and *H adsorbates, respectively. **(d)**, **(e)**, and **(f)** are front views of *OCHO, *COOH, and *H adsorbates, respectively. Cyan corresponds to an isosurface of −0.001 e Bohr^{-3} and yellow to +0.001 e Bohr^{-3}.

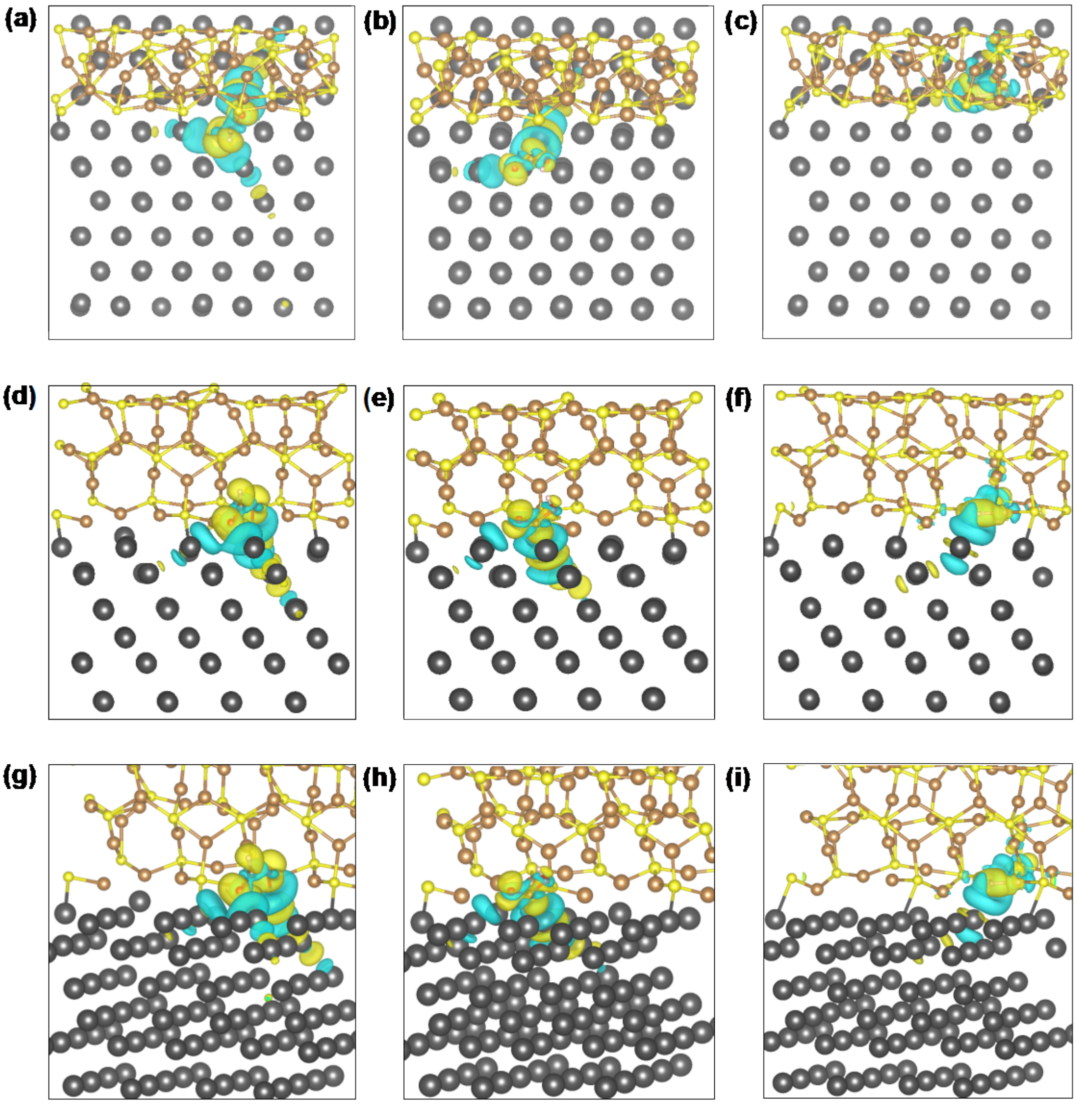

Figure S23. Isosurfaces of adsorbate-induced charge density difference for adsorbates on the Bi-Cu_2S interfacial surface. (**a**), (**b**), and (**c**) are top views of *OCHO, *COOH, and *H adsorbates, respectively. (**d**), (**e**), and (**f**) are front views of *OCHO, *COOH, and *H adsorbates, respectively. (**g**), (**h**), and (**i**) are side views of *OCHO, *COOH, and *H adsorbates, respectively. Cyan corresponds to an isosurface of −0.001 e $Bohr^{-3}$ and yellow to +0.001 e $Bohr^{-3}$.

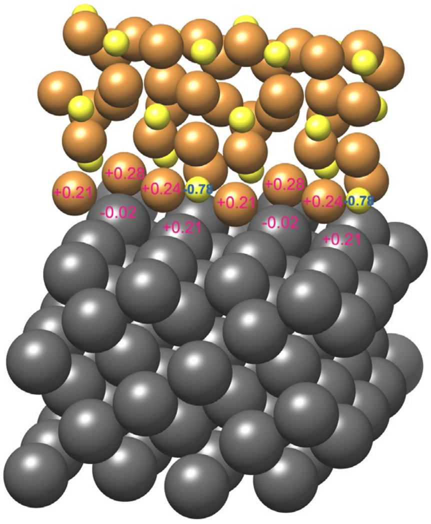

Figure S24. Bader charge analysis of the Bi-Cu_2S interfacial structure. Magenta values correspond to positive charges of atoms, and blue values correspond to negative charges of atoms.[17]

References

1. Zhang, Z.; Chi, M.; Veith, G. M.; Zhang, P.; Lutterman, D. A.; Rosenthal, J.; Overbury, S. H.; Dai, S.; Zhu, H., Rational Design of Bi Nanoparticles for Efficient Electrochemical CO2 Reduction: The Elucidation of Size and Surface Condition Effects. *ACS Catal.* **2016,** *6* (9), 6255-6264.

2. Zhai, Y.; Shim, M., Cu2S/ZnS Heterostructured Nanorods: Cation Exchange vs. Solution–Liquid–Solid-like Growth. *ChemPhysChem* **2016,** *17* (5), 741-751.

3. Tan, W.; Cao, B.; Xiao, W.; Zhang, M.; Wang, S.; Xie, S.; Xie, D.; Cheng, F.; Guo, Q.; Liu, P., Electrochemical Reduction of CO2 on Hollow Cubic Cu2O@Au Nanocomposites. *Nanoscale Research Letters* **2019,** *14* (1), 63.

4. Mun, Y.; Lee, S.; Cho, A.; Kim, S.; Han, J. W.; Lee, J., Cu-Pd alloy nanoparticles as highly selective catalysts for efficient electrochemical reduction of CO2 to CO. *Appl. Catal. B* **2019,** *246*, 82-88.

5. Davey, W. P., Precision Measurements of the Lattice Constants of Twelve Common Metals. *Phys. Rev.* **1925,** *25* (6), 753-761.

6. Buerger, M. J. a. W., B J, Distribution of Atoms in High Chalcocite, Cu2S. *Science* **1963,** *141* (3577), 276--277.

7. III, R. D. J. NIST Computational Chemistry Comparison and Benchmark Database. http://cccbdb.nist.gov/

8. Peterson, A. A.; Abild-Pedersen, F.; Studt, F.; Rossmeisl, J.; Nørskov, J. K., How copper catalyzes the electroreduction of carbon dioxide into hydrocarbon fuels. *Energy & Environmental Science* **2010,** 3 (9), 1311-1315.

9. Han, N.; Wang, Y.; Yang, H.; Deng, J.; Wu, J.; Li, Y.; Li, Y., Ultrathin bismuth nanosheets from in situ topotactic transformation for selective electrocatalytic CO2 reduction to formate. *Nat. Commun.* **2018,** *9* (1), 1320.

10. Rendón-Calle, A.; Builes, S.; Calle-Vallejo, F., Substantial improvement of electrocatalytic predictions by systematic assessment of solvent effects on adsorption energies. *Appl. Catal. B* **2020,** *276*, 119147.

11. Bohra, D.; Ledezma-Yanez, I.; Li, G.; de Jong, W.; Pidko, E. A.; Smith, W. A., Lateral Adsorbate Interactions Inhibit HCOO− while Promoting CO Selectivity for CO2 Electrocatalysis on Silver. *Angew.*

Chem. **2019,** *131* (5), 1359-1363.

12. Nørskov, J. K.; Rossmeisl, J.; Logadottir, A.; Lindqvist, L.; Kitchin, J. R.; Bligaard, T.; Jónsson, H., Origin of the Overpotential for Oxygen Reduction at a Fuel-Cell Cathode. *J. Phys. Chem. B* **2004,** *108* (46), 17886-17892.

13. Rossmeisl, J.; Chan, K.; Ahmed, R.; Tripkovic, V.; Bjorketun, M. E., pH in atomic scale simulations of electrochemical interfaces. *Physical Chemistry Chemical Physics* **2013,** *15* (25), 10321-10325.

14. Saitoh, K.-I.; Sato, T.; Takuma, M.; Takahashi, Y.; Chin, R., Molecular dynamics study on lubrication mechanism in crystalline structure between copper and sulfur. *J. Mater.* **2015,** *2015*, 1-13.

15. Stenlid, J. H.; dos Santos, E. C.; Johansson, A. J.; Pettersson, L. G. M., On the Nature of the Cathodic Reaction during Corrosion of Copper in Anoxic Sulfide Solutions. *J. Electrochem. Soc.* **2019,** *166* (6), C196.

16. Kashida, S.; Shimosaka, W.; Mori, M.; Yoshimura, D., Valence band photoemission study of the copper chalcogenide compounds, Cu2S, Cu2Se and Cu2Te. *J. Phys. Chem. Solids* **2003,** *64* (12), 2357-2363.

17. Tang, W.; Sanville, E.; Henkelman, G., A grid-based Bader analysis algorithm without lattice bias. *J. Phys.: Condens. Matter* **2009,** *21* (8), 084204.